ABSTRACT

Ps Receiver Function Imaging of Crustal Structure and Moho Topography Beneath the Northeast Caribbean

Gift Ntuli, M.S.

Committee Chairperson: Robert Pulliam, Ph.D.

The Caribbean plate consists of accreted different geologic terrains bounded by a system of complex plate boundaries. We conduct P-to-S receiver function studies of the Northeast Caribbean in order to image the plate boundary and study the major forces driving tectonics and strain distribution in the region. To calculate a velocity model for migration, we implement a technique analogous to "velocity analysis" in reflection seismology. We image a strong positive amplitude feature that shallows from ~40 km in the west to ~30 km in the east, which we interpret as the Moho. We also image a feature at ~80 km, which we conclude to be a subducting North America (NA) slab pushing against the Caribbean lithosphere. The next step in seismological studies of the Northeast Caribbean region is seismic tomography using teleseismic and local arrivals. This will allow us to gain insight into the volume and location of features

Ps Receiver Function Imaging of Crustal Structure and Moho Topography Beneath the Northeast Caribbean

by

Gift Ntuli, B.S.

A Thesis

Approved by the Department of Geosciences

Stacy C. Atchley, Ph.D., Chairperson

Submitted to the Graduate Faculty of
Baylor University in Partial Fulfillment of the
Requirements for the Degree
of

Master of Science

Approved by the Thesis Committee

Robert J. Pulliam, Ph.D., Chairperson

John A. Dunbar, Ph.D.

David Kahle, Ph.D.

Accepted by the Graduate School

August 2016

J. Larry Lyon, Ph.D., Dean

Page bearing signatures is kept on file in the Graduate School.

TABLE OF CONTENTS

LIST OF FIGURES

ACKNOWLEDGMENTS

I want to thank my parents for all the emotional support they continue to provide me with while I am thousands of miles away from home. I would also like to thank my advisor Dr. Pulliam who took me into his geophysics group and taught me the science and fun of geophysics. I am grateful for all the times he was available to answer my questions and challenge me to think critically. Most importantly, I am thankful for his calm, patient and understanding approach throughout my time at Baylor. It made all the difference. Likewise, I would not have made it without the support of all the members of the geophysics group at Baylor (both students and staff) and my committee members Dr. Dunbar and Dr. Kahle.

To my parents, Lewis and Gladys, and all the strangers who showed interest in my life and made me who I am today.

CHAPTER ONE

Introduction

The Caribbean plate, located between the North and South American plates, is considered to be one of the most complicated tectonic regions on earth (Giunta et al., 2003). The plate likely originated in the Pacific during the Cretaceous when magmatic events resulted in the formation of what is known today as the Caribbean large igneous province (Bezada et al., 2010; Coffin and Eldholm., 1994). It then migrated to its present day location as a result of two major collisions: first with the North American (NA) plate, at ~55–60 Ma, which resulted in a clockwise rotation of the plate (Pindell and Dewey, 1982), and then with the South American (SA) plate, from the Eocene to present day (Dewey and Pindell, 1986; Rosencrantz et al., 1988). These collisional events also resulted in the spatial and temporal juxtaposition of different geologic terrains and the formation of complex plate boundaries, comprised of deformed convergent, divergent and transform margins (Niu et al., 2007; Meighan and Pulliam, 2013). The roles and depth extent of the faults, as well as strain partitioning between the fault types—strike-slip and subduction, and their implications for seismic hazards in the region still remain unresolved.

In this paper we study the tectonics of the region using the P-to-S receiver function method to image the crust and upper mantle features in the Northern Caribbean Plate Boundary Zone (NCPBZ). Developed by Langston (1977), the receiver function method is sensitive to layer thickness and impedance contrasts, therefore applying the technique in the NCPBZ allows us to delineate the lateral extent and depth of crustal and upper mantle features. We compute P-to-S receiver functions from broadband seismic data obtained from 26 stations in Hispaniola. Then we migrate and stack the receiver functions in the depth domain to create a 3D volume of the subsurface of approximately 148 km N-S, 450 km E-W, and 200 km deep. Migration requires a seismic velocity model, for which we compute a local 3D, shear and compressional wave velocity model via "velocity analysis" in a fashion that is similar to the processing of reflection seismic data in the oil and gas industry. In our implementation we use a global optimization technique called Very Fast Simulated Annealing (VFSA) to find the 1D optimum velocity model beneath each of the 26 stations. We then interpolate the set of 1D models to create a 3D velocity model specific to the region. Using a constrained velocity model allowed us to place major impedance contrasts beneath the island of Hispaniola at their appropriate depths.

We evaluate our results against the mechanisms proposed by previous studies to explain the plate motion and tectonic forces at work along the NCPBZ. A better understanding of the NCPBZ subsurface features will enhance our capabilities to characterize the region for seismic hazards. Additionally, there are at least 30 other major plate boundaries similar to the NCPBZ, where the plate boundary transitions from subduction to strike-slip, but most such locations are offshore and are therefore more difficult to study (Mann et al., 2002). Our improved understanding of the tectonic setting in the NCPBZ will thus inform studies of similar tectonic regimes around the world that are less accessible.

CHAPTER TWO

Tectonic setting and Previous Studies

The NCPBZ is fragmented into three microplates: the Gonave microplate to the west (Rosencrantz and Mann, 1991), the Hispaniola microplate in the center (Mann et al., 2002), and the Puerto Rico-Virgin Islands microplate to the east (Byrne et al., 1985) (Figure 1). The region is bounded to the east by the westward subduction of the North America (NA) plate at the northern Antilles, which transitions to oblique subduction along the Puerto Rico Trench (van Benthem et al., 2013). North of Hispaniola, the plate boundary is dominantly strike-slip along the Septentrional fault and the North Hispaniola deformed belt (Dillon et al., 1992). Similarly, the western Caribbean boundary is defined by strike-slip motion at the Oriente and Swan transform fault zone (Dillon et al., 1992). The complex plate motion in the NCPBZ and the associated tectonic forces continues to be a subject of major debate.

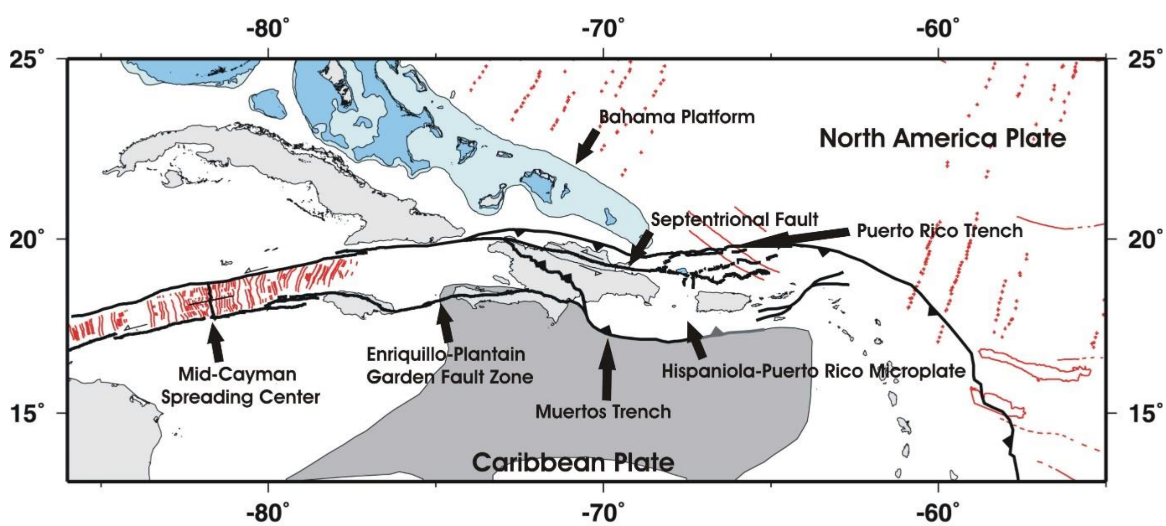

Figure 1. Map of the Northern Caribbean Plate Boundary Zone with major fault zones and geological features labeled. The red dots represent magnetic strips on the sea floor modified from Mann et al. (2003).

In previous studies, researchers proposed a variety of scenarios to explain the micro-plate motion, and crustal features believed to exist in the region. Van Benthem et al. (2014) suggested two mechanisms for plate boundary deformation in the region, the Bahamas collision and the slab edge push. In the first scenario the Bahamas carbonate platforms are colliding with the Caribbean plate resulting in unusually large earthquakes and fragmentation of the NCPBZ (Dolan and Wald, 1998; van Benthem et al., 2014). With the slab edge push theory, there is a torn edge of the NA plate located beneath Hispaniola between 69 and 70W associated with a subduction transform edge propagator (STEP). The westward propagation of the STEP with the NA plate is causing the Caribbean plate to deform to accommodate the strain (Figure 2; Govers and Wortel, 2005; van Benthem et al., 2014).

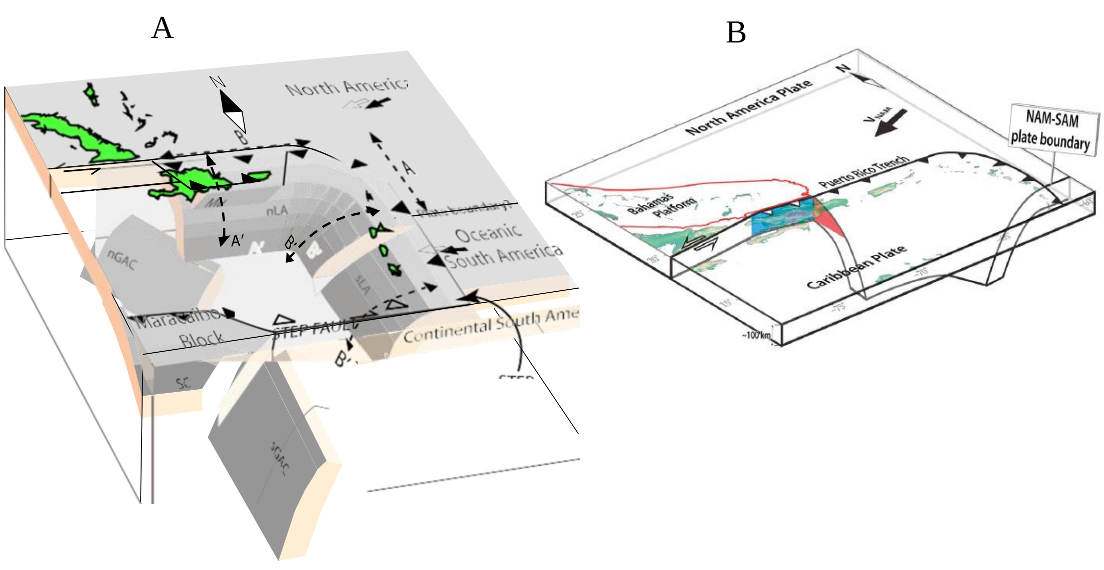

Figure 2. A. A three-dimensional rendering of the crustal and upper mantle structure in the eastern Caribbean as proposed by van Benthem et al. (2014). A westward subducting NA slab located beneath eastern Hispaniola is pushing against the dipping Caribbean plate. B. The figure below is a representation of the northeast Caribbean plate boundary slab geometry as viewed from the southwest. NA plate is subducting in an E-W direction at the Lesser Antilles and Puerto Rico Trench. The blue area represents the contact region where the Bahamas platform is pushing against the Caribbean plate. The region where NA slab edge exerts a westward push on the Caribbean plate is denoted in red. Van Benthem et al. (2014) argues that Slab Edge Push is the major force driving deformation in the northeast Caribbean.

Another scenario was proposed by Calais et al. (1992), in which the Bahamas platforms are inhibiting subduction to the north and east of Hispaniola, causing the subducting NA plate to detach along the Septentrional fault in a zipper-like fashion (Figure 3). The last scenario is that the NA plate is subducting beneath Hispaniola and interacting with the northward dipping Caribbean slab to result in pockets of earthquakes to depths of ~200 km beneath Hispaniola (Figure 4; Dolan et al., 1998; Mann et al., 2002). These are all viable scenarios; evaluating them requires more data and modeling to support or refute each scenario's implications. Previous studies of the crustal and upper mantle features in the Caribbean have utilized geophysical methods like tomography (e.g., van Benthem et al., 2014) and anisotropy (e.g., Meighan et al., 2013), but questions surrounding the existence and roles of the features in regional tectonics remain unsolved.

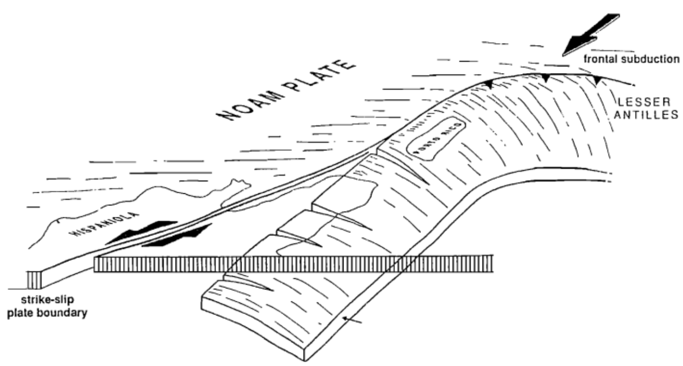

Figure 3. Cartoon illustrating the proposed idea by Calaise et al., (1992) to explain the role of the Bahamas platforms in the tectonics of the northeast Caribbean. Obstruction of movement by the Bahamas platform is causing the NA plate to "zip" open beneath Hispaniola.

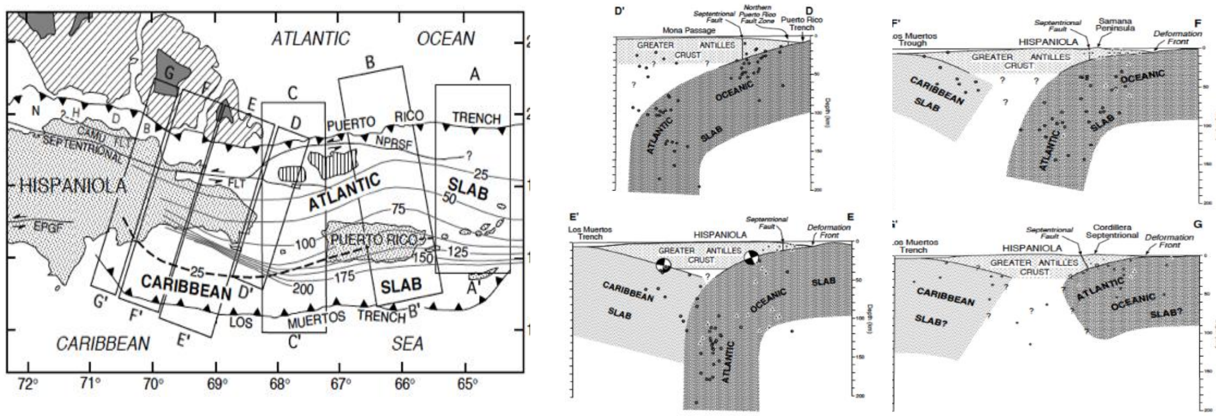

Figure 4. N-S cross-sections across the NCPBZ demonstrating Dolan et al.'s (1998) theory that the southward subducting NA slab is interacts with the northward dipping CAR slab to result in pockets of earthquake at depth beneath Hispaniola (E-E'). As we progress westward (F-F' and G-G') there are no earthquakes because the CAR and NA slabs aren't yet in contact. Likewise, to the east (D-D'), the NA plate is intact beneath the Mona Passage resulting in the absence of earthquakes.

CHAPTER THREE

Data

The dataset used in this experiment mainly comprise P- and PP-wave events having magnitude > 5.5 at epicentral distances of 30°-90°. Events were recorded by a total of 26 stations mainly consisting of the Greater Antilles Seismic Program (GrASP) network, which was installed in the summer of 2014 as a collaboration between Baylor University, the National Center for Seismology (CNS), an organized research unit within the Autonomous University of Santo Doming (UASD, Dominican Republic), and the Puerto Rico Seismic Network (PRSN) (Figure 5). Each station consists of a three-component Nanometrics Trillium Compact seismometer and a Reftek 130 digitizer/recorder. The equipment is powered by a solar charged battery and data are streamed in real time using cellular telemetry to CNS in Santo Domingo and to Baylor and the IRIS Data Management Center from CNS via the Internet. We also obtained data from permanent stations located on the island of Hispaniola that are operated by the Puerto Rico Seismic Network (PR), the Canadian Seismic Network (CN), the U.S. Geological Survey's Caribbean Network (CU), and the Haitian Seismic Network (AY). All of these additional stations were installed between 2000 and 2013 and remain in operation, so we were able to obtain more extensive sets of records for them than for stations of the temporary GrASP network. After preprocessing and manual inspection to cull events with low signal-to-noise ratio and/or SV-dominant polarization, the final dataset of 1755 broadband seismograms was used to compute receiver functions.

Figure 5. Map of the stations used in the study (red) and location of events used (blue). The events were selected such that the data covered a wide epicentral distance.

Methods

The receiver function method relies on the conversion of waves incident upon a sharp discontinuity (impedance contrast) beneath a recording station, either from P- to S-type (PRFs) or from S- to P-type (SRFs) (Langston., 1979; Sodoudi et al., 2006). This results in a time delay between the arrivals of direct and converted waves, which is dependent on the depth to the converting discontinuity, shear and compressional velocities of the layers above the impedance contrast, and ray parameter of the converted waves (Sodoudi et al., 2006). Kind and Vinnink. (1988) showed that by modeling the impedance contrast above a boundary as a single layer over a half space and treating the direct and converted phases as travelling waves as plane waves with the same ray parameter values (Figure 6) , we can calculate the delay time for P-to-S as:

$$\Delta t = t_{P_S} - t_{P_P} = H\left(\sqrt{\frac{1}{\beta^2} - p^2} - \sqrt{\frac{1}{\alpha^2} - p^2}\right), \quad (1)$$

Where t_{P_P} and t_{P_S} are the travel times for the direct and converted waves from the boundary of impedance contrast, p denotes the ray parameter, α and β are the P- and S-wave velocities, and H is the depth of the discontinuity. Similarly, the PPS crustal reverberations consist of two P lags and one S lag (Figure 6). Therefore, its delay time is calculated as:

$$\Delta t = t_{P_P P_S} - t_{P_P} = H\left(\sqrt{\frac{1}{\beta^2} - p^2} + \sqrt{\frac{1}{\alpha^2} - p^2}\right), \quad (2)$$

Although we computed both P and S receiver functions, we ended up using the P-to-S type only. Due to a combination of low station coverage and a smaller epicentral distance window, the set of recorded events did not yield enough good SRFs to image features reliably.

Ps waves consist of higher frequency signals because they originate with P-waves, which are richer in high frequencies than S-waves, and they suffer less path attenuation at teleseismic distances than S-waves (Hansen and Dueker, 2009). As a result, images produced via PRFs are of higher spatial resolution compared to SRFs (Yuan et al., 2006). Another advantage of PRFs is that they have a higher data fold due to a wider epicentral distance range (Wilson et al., 2006; Yuan et al., 2006). S receiver functions have a restricted range of epicentral distances under which S-to-P waves are recorded without being degraded by secondary arrivals. In the following sections we first discuss receiver function computation, then velocity analysis, and finally migration and stacking.

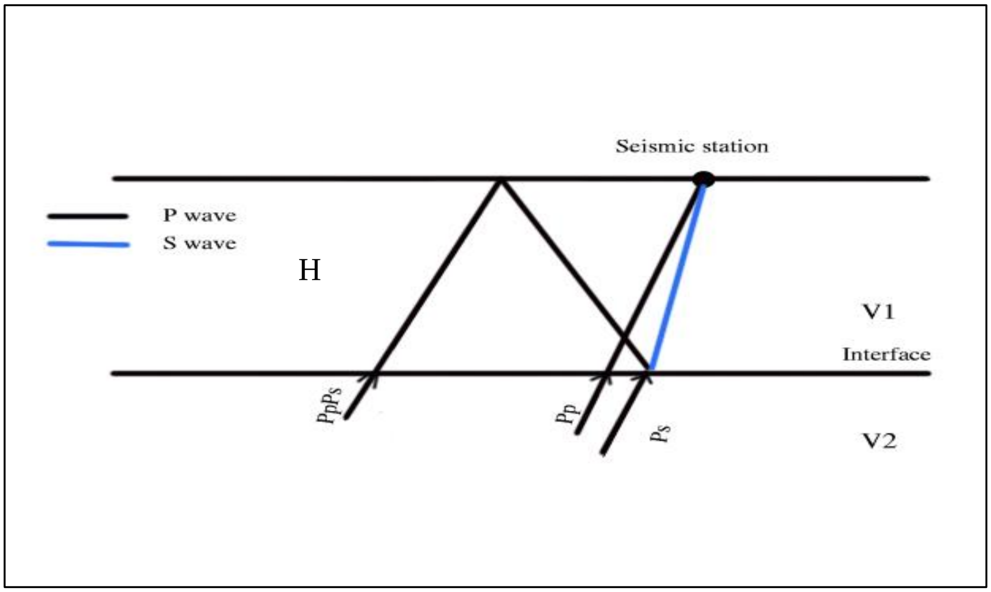

Figure 6. P waves incident upon a half space Part of the P-wave energy is converted into S-wave energy. The PpPs crustal reverberations consists of two P lags and one S lag. See text for further details. The difference in travel times, t_{P_P} and t_{P_S} result in a delay time. See text for further details.

1. Receiver Function Computation

Receiver functions are computed using a two-step process: coordinate rotation followed by deconvolution (Langston., 1977; Li et al., 2004). First we window seismograms to a duration 30 seconds before and 150 seconds after the direct P wave arrival, then bandpass filter the data with corner frequencies of 0.02 and 2 Hz. Next, we rotate seismograms from the ZNE to the ray-based ZRT coordinate system as shown in equation (3), to isolate the converted P-to-S energy from the direct arrivals (Vinnik, 1977; Amukti et al., 2015).

$$\begin{pmatrix} R \\ T \\ Z \end{pmatrix} = \begin{pmatrix} cos\theta & sin\theta & 0 \\ -sin\theta & cos\theta & 0 \\ 0 & 0 & 1 \end{pmatrix} \begin{pmatrix} E \\ N \\ Z \end{pmatrix}, \quad (3)$$

In the ZRT coordinate system, the direct P and PP phases are prominent on the vertical (Z) component, whereas SV waves, such as converted P-to-S waves, are dominant on the radial (R) component (Yuan et al., 2000). The incident angle for rotation (θ) is determined by minimizing the S-component for P arrivals (Vinnik, 1977).

Receiver functions are then computed via deconvolution to remove the effects of the source, ray path and instrument response from the seismograms (Yuan et al., 2000). We implement an iterative deconvolution technique in the time domain as described by Ligorria and Ammon (1999) to deconvolve the P signal on the Z component with the SV phase on the R component. In this method, first an estimate of the largest spike in the receiver function is made by cross-correlating the vertical component with the radial component. The spike's amplitude is calculated using an equation by Kikuchi and Kanamori (1982). Then the current estimate of the receiver function is convolved with the vertical component of the seismogram and the result is subtracted from the radial component. The procedure is iterated to estimate other amplitudes of the receiver function. As more spikes are added to the receiver function estimate, the misfit between the radial component and the vertical and receiver function convolution decreases. This process is repeated until the misfit is insignificant.

A low-pass Gaussian filter is applied to remove high frequency noise in the receiver functions and is described by the equation

$$G(w) = e^{-\frac{w^2}{4a^2}}, \quad (4)$$

where a is the Gaussian width factor and w is the angular frequency (Ligorria and Ammon, 1999). The filter width parameter controls the bandwidth of the receiver functions, which determines the limits of resolution of layer thickness. The larger the filter width parameter, the larger the signal bandwidth. We use a Gaussian width factor of 2.0 and allow each receiver function estimation to run for 300 iterations or until the misfit between the vertical and receiver function convolution and the radial component seismogram is 0.01%, whichever comes first. We compute receiver functions for 10 seconds before and 50 seconds after the arrival of the direct wave. Then we manually select receiver functions that showed a clear direct arrival followed by a converted wave within 5 seconds whose amplitude was at most 50 percent that of the direct arrival. Using this criterion, a total of 655 P-to-S and PP-to-S receiver functions were computed (Figure 7).

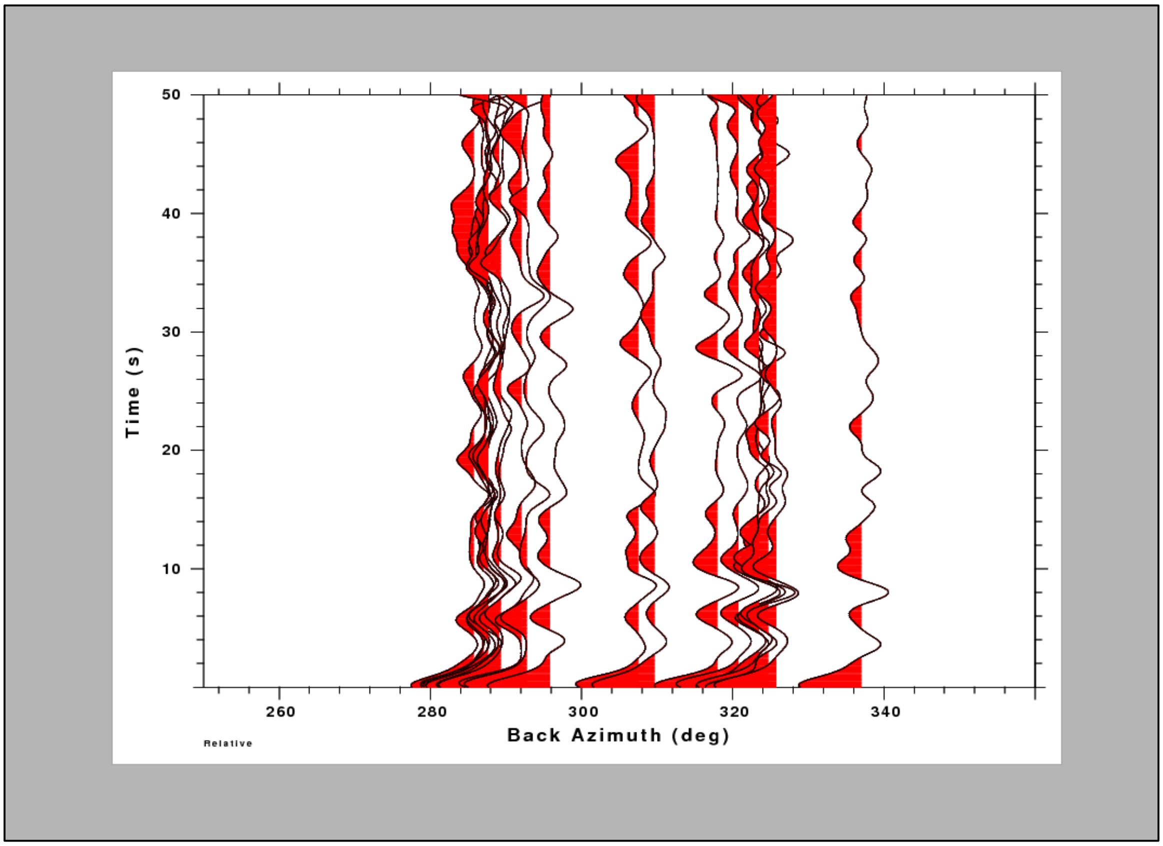

Figure 7. An example of what the final receiver functions looked like. This image is for receiver functions computed for station SDDR plotted against back azimuth from 0- 360^{o}

2. Velocity Analysis

We compute our receiver functions in the time domain, but need to migrate and stack them in the depth domain to correct dip angles of features and convert delay times to depths (Agrawal et al., 2015). Migration requires a velocity model and in the past, researchers utilized a general velocity model called ak135, which increased the chances of subsurface features being placed at inappropriate (shallower or deeper) depths. We address this problem by optimizing the ak135 velocity model to generate a new velocity model specific to our study region. This is accomplished using a two-step process driven by a global optimization technique called Very Fast Simulated Annealing (VFSA) (Kirkpatrick et al., 1983; Agrawal et al., 2016).

VFSA is a variant of simulated annealing (SA), which was first proposed by Szu and Hartley (1987) to address the problem of efficiency associated with the original method (Sen and Stoffa., 1995; Vakil-Bagmisheh et al., 2008). Simulated annealing creates an analog between an annealing metal and numerical optimization problems (for applications in seismology, see Agrawal et al., 2016). For example, a liquid metal at initial temperature (T_0) if gradually cooled will go through various crystal rearrangements at each temperature until it finally reaches the best-organized crystal structure also known as the ground energy state (Sen and Stoffa., 1995; Agrawal et al., 2015). Likewise, the simulated annealing algorithm starts with an initial temperature (T_0), which is decreased at each iteration (k), by an amount determined by a cooling schedule($T\ (k)\ =\ T_0/k$). At each temperature, an updated model is randomly selected from a distribution within a model parameter space specified by the user (Agrawal et al., 2016). In our case we varied the model space's Poisson's ratio, shear wave velocities and thickness of each layer.

Unlike the Metropolis algorithm, which derives model parameters from a uniform distribution, VFSA uses a Cauchy-like distribution to generate model parameters (Szu and Hartley, 1987; Sen and Stoffa, 1995). This allows VFSA to search the model space broadly during initial iterations at higher temperatures, and once it has identified regions that contain global maxima (at lower temperatures) it narrows its search to define local minima more exactly, which makes it computationally fast and efficient (Geman and Geman, 1984; Szu and Hartley, 1987).

Figure 8 explains how we implement the Very Fast Simulated Annealing algorithm to optimize velocity models in this study. During each iteration, we migrate receiver functions for the current station from the time to the depth domain using the new velocity model drawn during that current iteration (m^{new}), and delay time calculated using equation (1). The migrated receiver functions are then stacked to obtain a master trace, which we then cross-correlate with each individual receiver function. We used the objective function below to calculate average normalized cross-correlation value (CC_j) for the jth seismic station as

$$CC_j = \frac{\Sigma_i^N S \otimes t_i}{N_j}, \quad (5)$$

where the cross-correlation function denoted by the $\otimes$ operator is acting on the master trace S and the i^{th} receiver function, t_i. N_j is the total number of receiver functions. Equation (5) in generalized form can be written as:

$$CC_k = \frac{\Sigma_{j=1}^{N_k} \frac{\Sigma_k t_{rm}^k . t_r^{j,k}}{\sqrt{\Sigma_k t_{rm}^k . t_{rm}^k} \sqrt{\Sigma_k t_r^{j,k} . t_r^{j,k}}}}{N^k}, \quad (6)$$

Where $t_r^{j,k}$ and t_{rm}^k represent the j^{th} receiver function of the gather for station k, and the

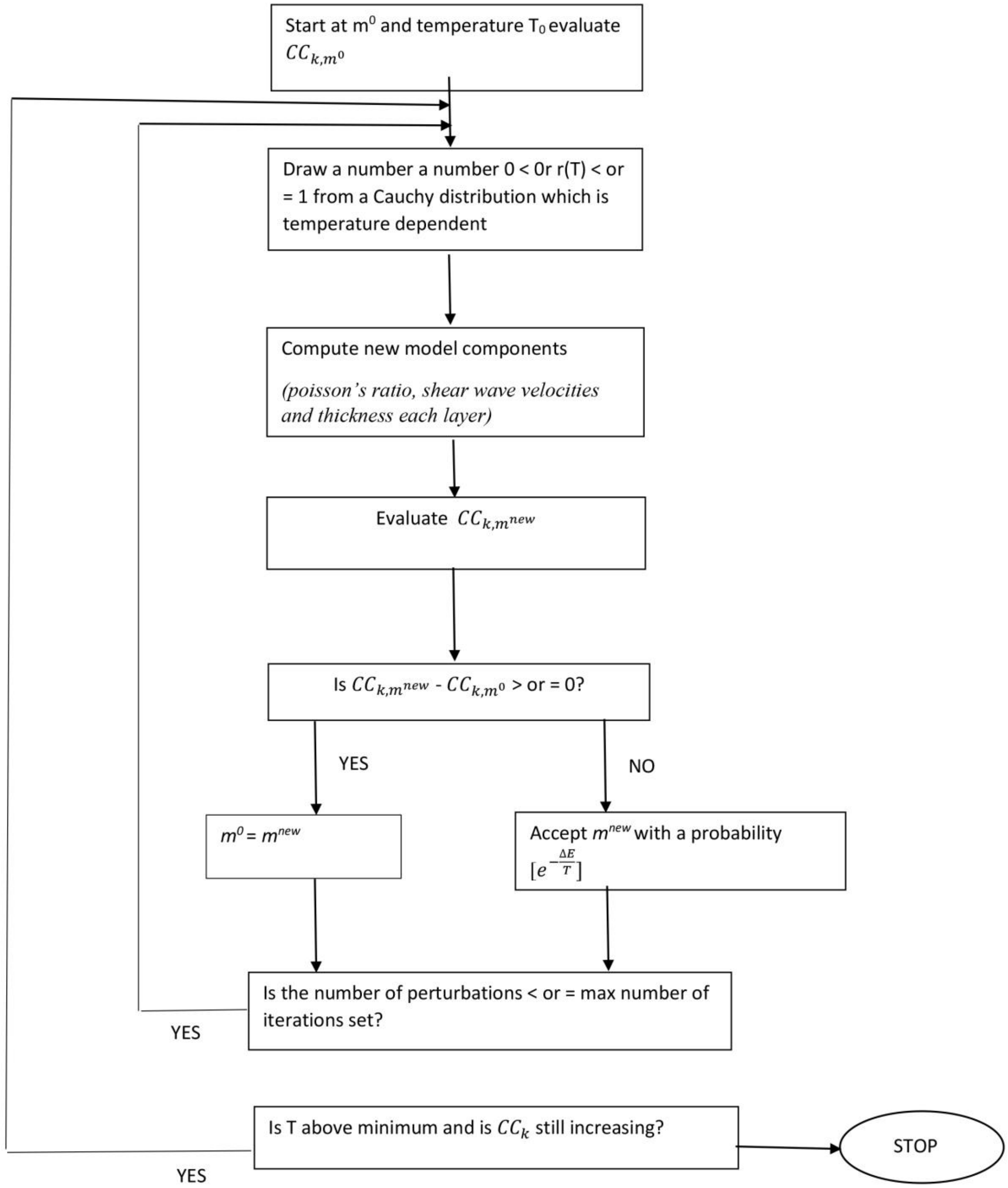

Figure 8. Flow chart explaining the Very Fast Simulated Annealing algorithm used to optimize the velocity models in this study (Modified from Gangopadhyay et al., 2007 and Sen and Stoffa 1995). $CC_{k,m^{new}}$ is the normalized cross-correlation value computed using the new velocity model, m^{new}, which is then compared to the normalized cross-correlation value CC_{k,m^0} computed from the previous model, m^0. See text for further details.

corresponding master stacked receiver function trace respectively. The total number of receiver functions at station k is represented by N^k. The normalized cross-correlation value associated with the new model $\left(CC_{k,m^{new}}\right)$ is compared to the normalized cross-correlation value obtained using the previous best velocity model (CC_{k,m^0}). If $CC_{k,m^{new}}$ is equal or greater than CC_{k,m^0} then the current velocity model is accepted and replaces the previous model. However, even if $CC_{k,m^{new}}$ is less than CC_{k,m^0}, the latter might still be accepted with a probability $[e^{-\frac{\Delta E}{T}}]$, where ΔE is the change in energy and T is the temperature (Sen and Stoffa, 1995; Vakil-Bagmisheh et al., 2008). Thus, the probability of accepting up-hill moves (normalized cross-correlation values smaller than the last one) is greater when the temperature is still high and decreases with lower temperatures (Vakil-Bagmisheh et al., 2008). This characteristic also means that VFSA does not require an initial model near the solution, which enabled us use the global model ak135 as our starting model. More details on VFSA can be found in Sen and Stoffa (1995).

We computed individual 1D velocity models for shear wave velocities to a depth of 200 km beneath each of the 26 individual stations. For each station, we input the ak135 velocity profile and then vary Poisson's ratio and shear velocity for the crust and mantle between ±5% and ±3% respectively. The thickness of each layer is allowed to vary between ±10% for the crust and ±20% for the mantle. We set the initial temperature at 10^{-4} dimensionless units and cool it to 10^{-15} units. We set the number of iterations to 500 because, during a series of tuning runs, we did not achieve significant improvements in the objective function at iterations beyond that number.

Next, we use the Poisson's ratio and shear wave velocities for each station to obtain the 1D compressional wave velocity model. All 26 compressional and shear wave velocity models are interpolated to generate result in a 3D velocity model for the whole study region.

3. Stacking And Migration

Receiver functions sharing ray paths can be stacked to increase the coherent signal energy and suppress noises (Zhu et al., 2000). Therefore, in the last step of our methodology we used the 3D velocity model from Step 2 to migrate and stack our receiver functions in a process called Common Conversion Point (CCP) stacking, which is analogous to Common Midpoint (CMP) stacking of reflection seismic data in the oil and gas industry (Kosarev et al., 1999; Dueker and Sheen, 1998). First we calculate ray paths of all our receiver functions using our 3D velocity model from Step 2. Then we calculate the delay times of all elements of each receiver function relative to its direct arrival using equations (1) and (2). Using the delay times, we back-project the receiver function along the ray path to the appropriate location at which the wave type conversion occurred.

This is similar to the migration performed in oil and gas exploration, but instead of locating reflectors in depth profiles, we are pinpointing the location of the impedance contrast below the recording seismic station using transmitted waves. Next, we divide the volume beneath our seismic stations into 3D bins and sum the amplitudes that fall in the same bin to obtain the average amplitude value of each bin (Figure 9). The receiver function's wavelength determines the horizontal dimensions of the bin size, whereas the vertical dimensions are determined by the sample interval of the receiver functions (Zhu et al., 2000).

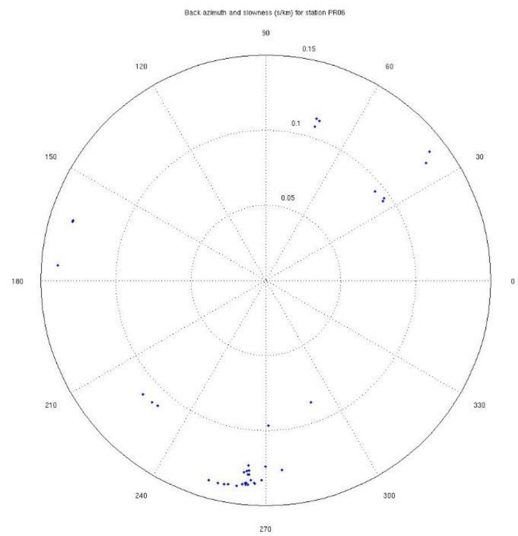

Figure 9. For each station the receiver functions were distributed in azimuthal bins before stacking. This image shows the bin distribution for station SDDR

For this study, we use a bin size of 30 km laterally (latitude and longitude) and 10 km in depth. This allows our bins to overlap and create smooth 3-D stacked and migrated images.

CHAPTER FOUR

Results

Figure 10 shows the locations of E-W cross-sections of the migrated and stacked images, of seismic stations used in this study, and of recent local earthquakes with well-constrained locations. (Local earthquakes were not used to compute receiver functions; they are shown here and in the subsequent figures for purposes of interpretation.) It is important to note that receiver functions do not give us information about the volumetric velocity variations of the subsurface; they reveal impedance contrasts that mark boundaries between subsurface features.

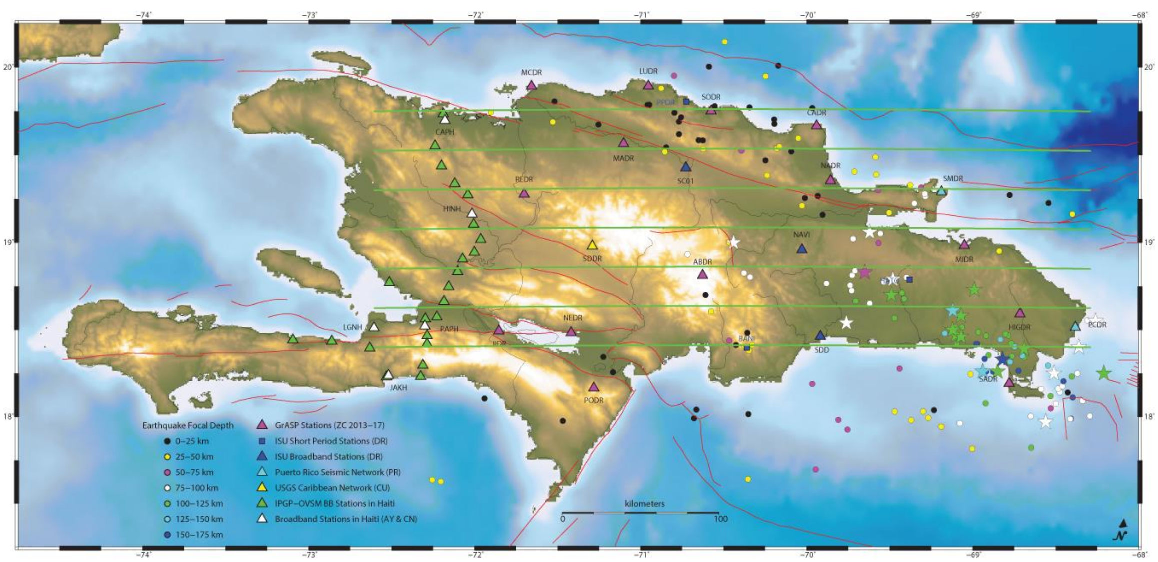

Figure 10. Locations of 2D slices shown in subsequent figures of the 3D migrated and stacked receiver function image. Most of the features on the map are explained in the key at left except for the red lines, which are major faults in the regions, and the white washed regions, which are areas of high elevation. Earthquakes epicenters shown with circles are from the Engdahl et al. (1999) Centennial catalog (colors indicate focal depth). Earthquakes epicenters shown with stars were recorded by the GrASP network between 2013-2016 and were re-located by Mejia et al. (2016).

A medium’s impedance is defined to be the product of the medium's density and its P-wave velocity. Positive polarity contrasts (purple and blue colors) represent an abrupt increase in impedance with depth, whereas negative polarities (yellow and red) indicate a decrease in impedance with depth. Since density tends to vary much less dramatically than seismic velocity in common Earth materials, impedance changes typically serve as proxies for changes in velocity. However, the topmost purple anomaly in all the images is the positive pulse of the direct P-wave arrival, not an impedance contrast.

In all cross-sections (Figures 11-17) a major positive polarity feature extends eastward at a depth of ~40 km beneath Western Hispaniola. At ~69.75°W longitude, this feature either steps down to a depth of approximately 50 km, or it steps up to a shallower depth of ~30 km. From the north of the island to ~ 18.75°N, this feature is continuous across leading to the step, but in the southern part of the island, the step is separated by a gap delineated by a swarm of earthquakes, which are denoted by red dots in cross-section A-A' (Figure 11). There is another positive amplitude impedance boundary located at ~130 km extending from eastern Hispaniola to ~69.40°W longitude. However, unlike the first positive amplitude feature at ~40 km, which extends across the western portion of the island, this second feature appears only in the east and there are no recorded earthquake hypocenters activity in its vicinity.

The two other prominent feature across all slices are negative polarity boundaries, one at ~82 km and the second at ~120 km. The bottom feature extends from ~71.25°W to ~70.00°W longitude, which is approximately where the upper feature begins and disappears at ~68.75°W longitude. Although the two impedance anomalies appear to be similar in size and amplitude, a key distinction is that the shallower feature at ~82°W is accompanied by a swarm of earthquakes (Figure 12; Figure 13), whereas there is no recorded seismicity associated with the bottom feature at ~120 km depth. Even though there are other anomalies in the cross-sections, we focus only on major impedance contrasts displaying strong amplitudes on multiple CCP slices. The fainter, inconsistent features may be processing artifacts arising from multiples, the simultaneous deconvolution technique we employ, or interpolation and smoothing. A general observation we make for all our cross-sections was that the quality of the image decreases from north to south; all boundaries in the cross-sections get fainter from north to south. For example, the resolution of the negative polarity features decreases from being two resolvable features (lines G-G' to D-D') to almost being one feature in A-A'. Figure 11-17. Cross-sections generated using migrated and stacked PRFs for the area of Hispaniola. In cross section F-F' and G-G', we cut the areas offshore because there are no station, which means that section of the images are not well constrained. The red dots in each image represent earthquakes whose hypocenters were located half a degree latitude above or below the location of the corresponding cross-section. We also plotted the topography and gravity measurements along each of the seven lines. Cross-section A-A' is the southernmost profile and G-G' is the northernmost.

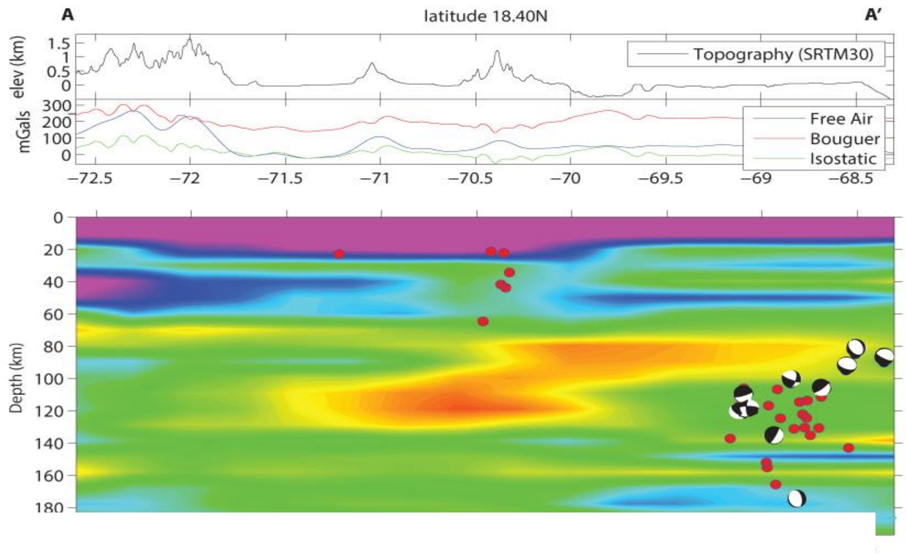

Figure 11. Profile A-A’

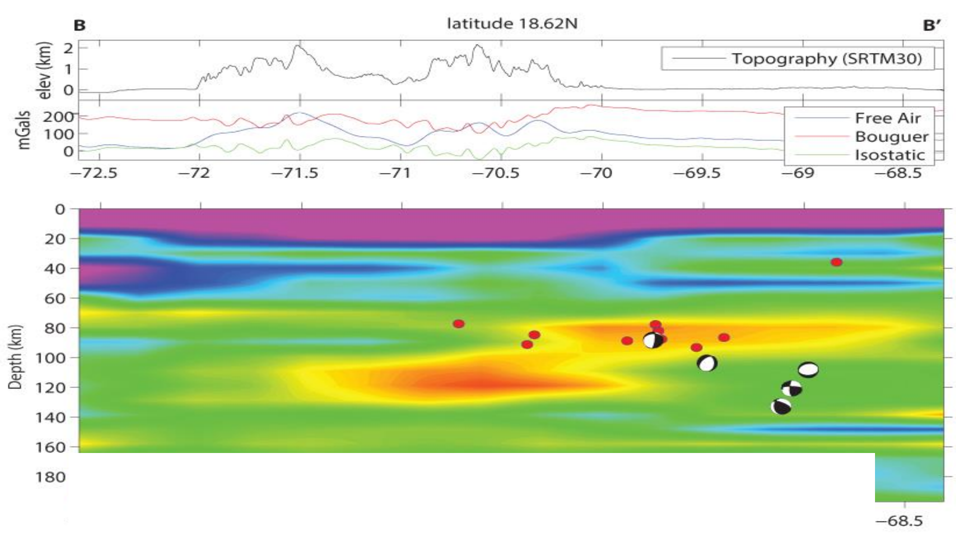

Figure 12. Profile B-B’

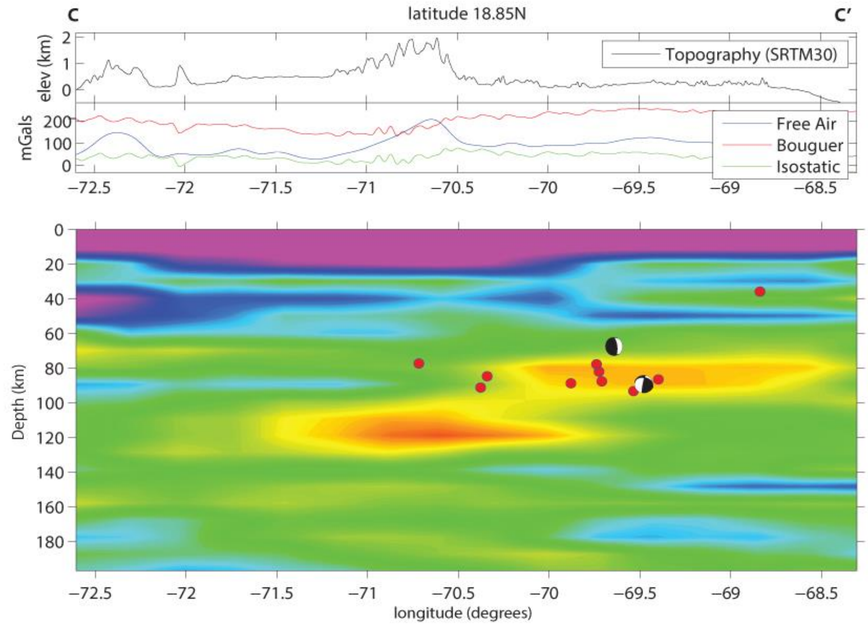

Figure 13. Profile C-C'

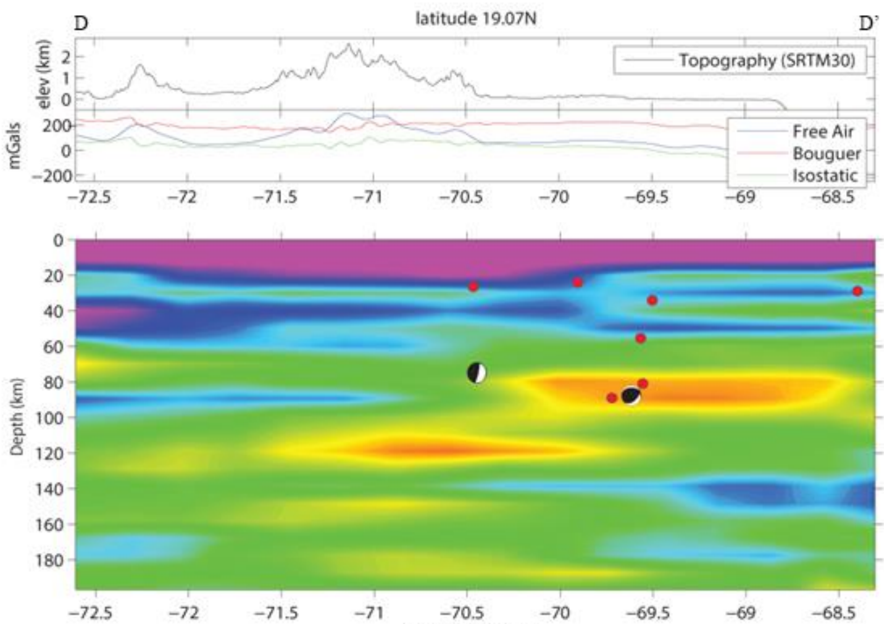

Figure 14. Profile D-D'

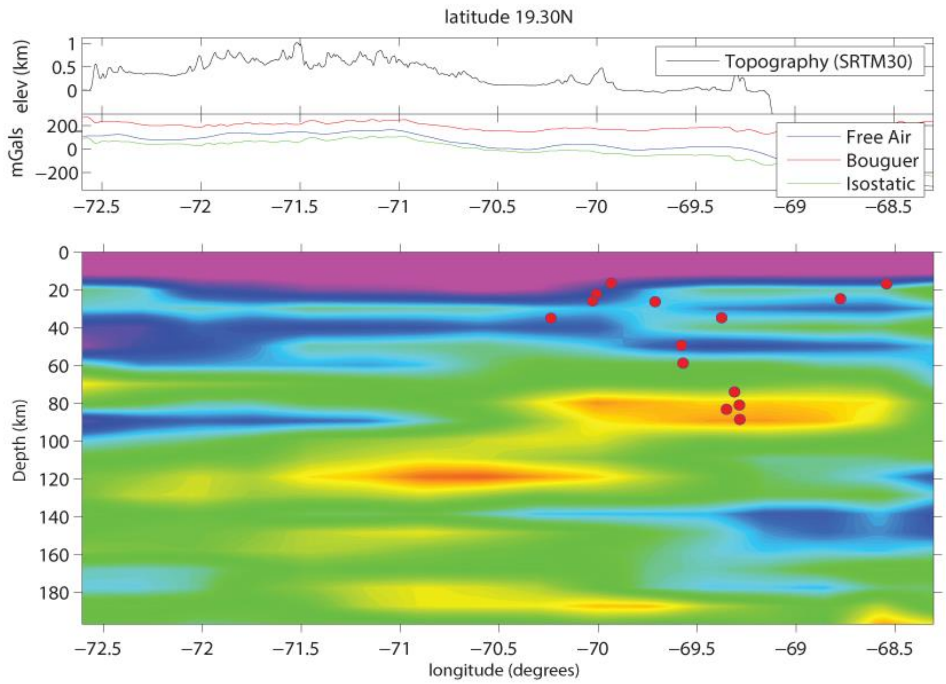

Figure 15. Profile E-E’

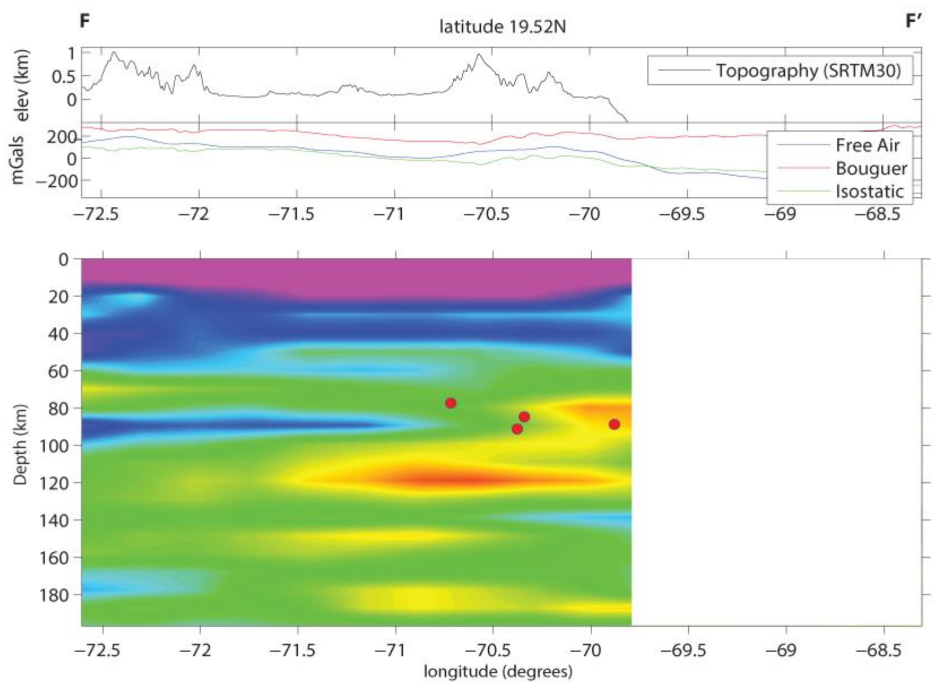

Figure 16. Profile F-F’

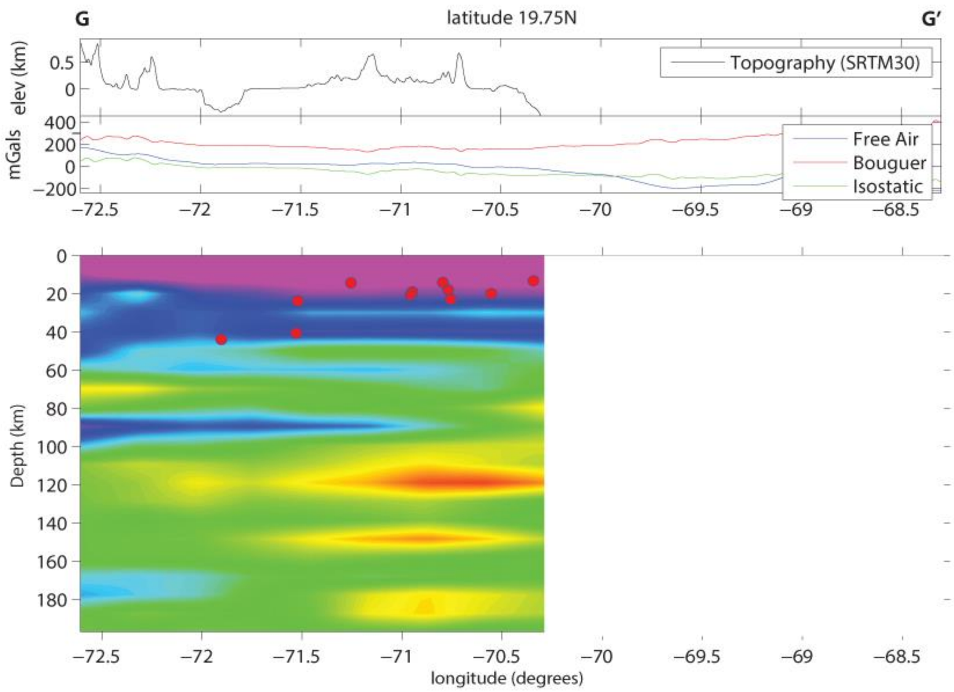

Figure 17. Profile G-G’

CHAPTER FIVE

Discussion

We interpret the positive amplitude feature at ~40 km in the west as the Moho, which shallows to ~30 in the east as a result of two mechanisms. The first mechanism is the upward thrust by the NA slab subducting beneath. The second mechanism is crustal thinning on the edges of Hispaniola (Figure 18). The latter is consistent with previous studies by Boynton et al., 1979, which indicated that on islands the crust is thick at the center and thins at the edges. We investigate the break in the Moho between ~70.75° W and ~70.00° W by looking at ray coverage in that region and as shown in Figure 21, the ray coverage is relatively low in the region where the Moho is missing. Given that the Moho is continuous in cross-sections C-F, to the north, and discontinuous in only the two most southerly cross-sections (A and B), we conclude that the lower ray coverage may produce a break in the Moho in A-A’ and B-B’ as an artifact of weaker constraints. The longitudinal location of the positive and negative anomalies at ~50 km and ~82 km respectively is consistent with where the subducting NA slab has been proposed by van Benthem et al. (2014), therefore we interpret the features as the top and bottom contact of the NA slab (Figure 2; Figure 18). Note that this feature coincides with a set of earthquakes in cross-sections B-B’, C-C’, D-D’, and E-E’, which might result from lithospheric tearing. Earthquakes at longitude ~69.00° W in A-A’ correspond with the region which Gudmundsson and Sambridge (1998) mapped as the Benioff zone for the NA-CA plate subduction zone. However, the events fall below the negative polarity event that we presume marks the lower bound of the NA lithosphere.

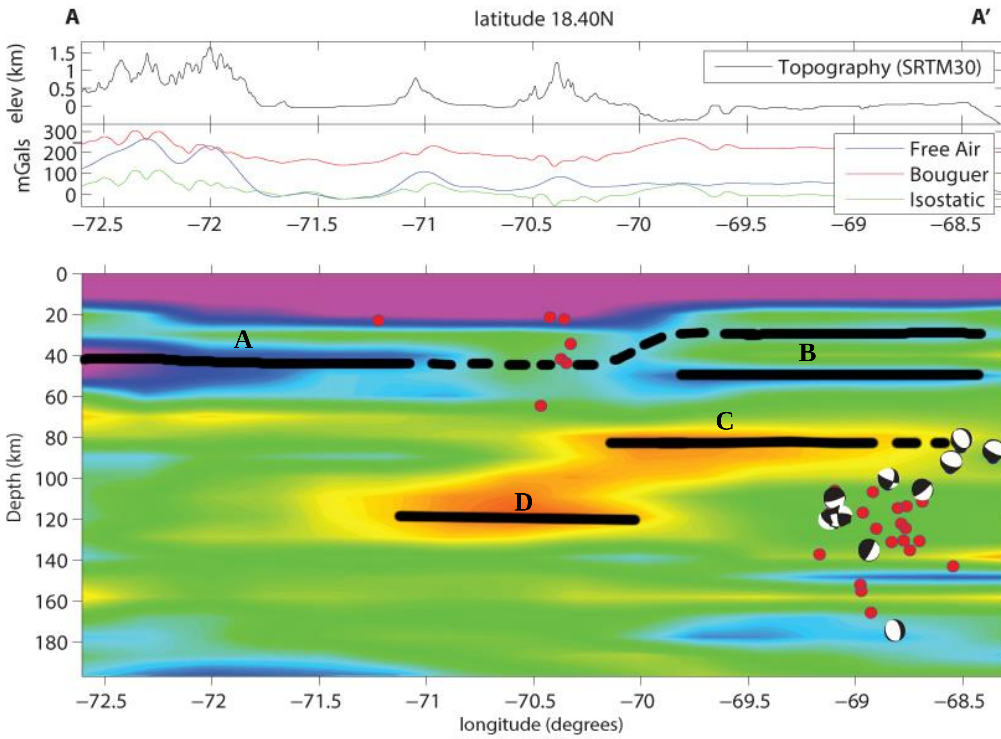

Figure 18. Interpreted image with the major discontinuities highlighted. A is the Moho which starts at a depth of ~40 km to the west and shallows to ~30 in the east as a result on being pushed from underneath by the NA slab. B and C are the upper and lower contacts of the subducting NA slab respectively. D is Lithosphere Asthenosphere Boundary (LAB) station density

Therefore, it is also possible that the events could be supportive of Dolan et al's (1998) theory that the southward subducting NA slab interacts with the northward dipping CAR slab to result in pockets of earthquake at depth (Figure 4; Figure 18). An alternative interpretation is that the hypocenters of the earthquakes in cross-sections A-A' and E-E' can be divided into two groups: shallow and deep seismicity. This is consistent with Calais et al.'s (1992) conclusion that the seismic activity in Northeast Caribbean results from two mechanisms: Earthquakes shallower that 50 km are produced by strike slip motion along the Septentrional fault, whereas deep earthquakes beneath Northeastern Caribbean. The latter cannot be directly associated with active faults, are as a result of a detached North American slab. In that case we should be able to image the lithospheric slab, of which we do not so more data is required to either support or refute this claim. We identified the impedance contrast at 120 km between longitudes 70W and ~71.5W as the Lithosphere-Asthenosphere Boundary (LAB) because it has the correct polarity and the expected depth.

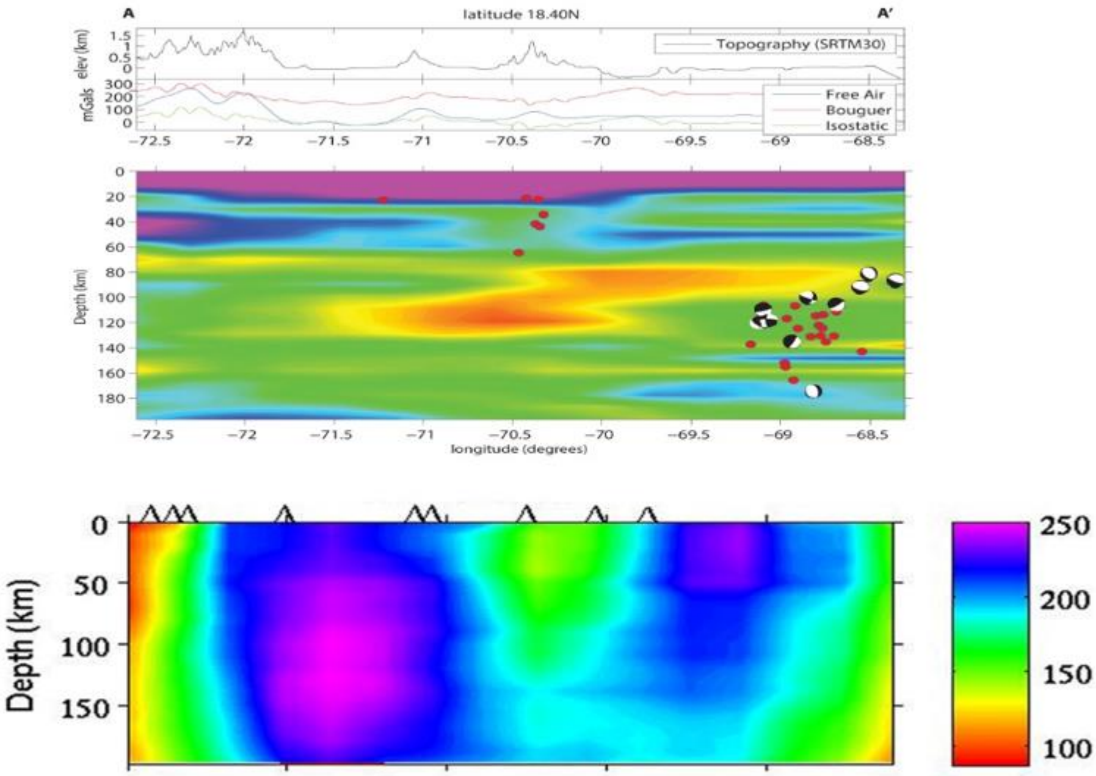

Figure 19. Hit count across profile A-A'. Hit count is a measure of ray density in the region, which is proportional to resolution of the stacked image. A lower hit count means less rays to be bin and stack which can result in features being degraded in corresponding regions of the image.

To study the relationship between surface topography and subsurface structure, we plotted elevation, free air and Bouguer gravity anomalies along the cross-sections. As expected, the gravity measurements correlate with topographic features. Additionally, we also noticed that the late P-wave arrivals (the dip in the top purple layer across all cross-sections) occurred in the highlands region in central Hispaniola (map, B-B', C-C', D-D', E-E').

Figure 20 is a cartoon representation of our final interpretation of the structural boundaries beneath Hispaniola. In this interpretation, the encroaching NA lithosphere is pushing against CAR plate as it subducts beneath northeastern Hispaniola. As a result, the Caribbean lithosphere is experiencing deformation, which is causing the uplift occurring in central Hispaniola. As shown by the gravity and topography, the island has relatively low elevations in the east but changes dramatically at longitude ~70.25°W, which is where the NA slab starts pushing against the Caribbean lithosphere (Figure 18; Figure 20). We propose that the subducting NA lithosphere and its end (marked by the set of earthquakes in cross-section B-B' and C-C') give rise to the slab edge push proposed by van Benthem (2014) (Figure 2; Figure 20). Therefore, we also conclude that slab edge push is the major driving force behind deformation in the northeast Caribbean region, which is consistent with van Benthem et al.'s (2014) conclusion.

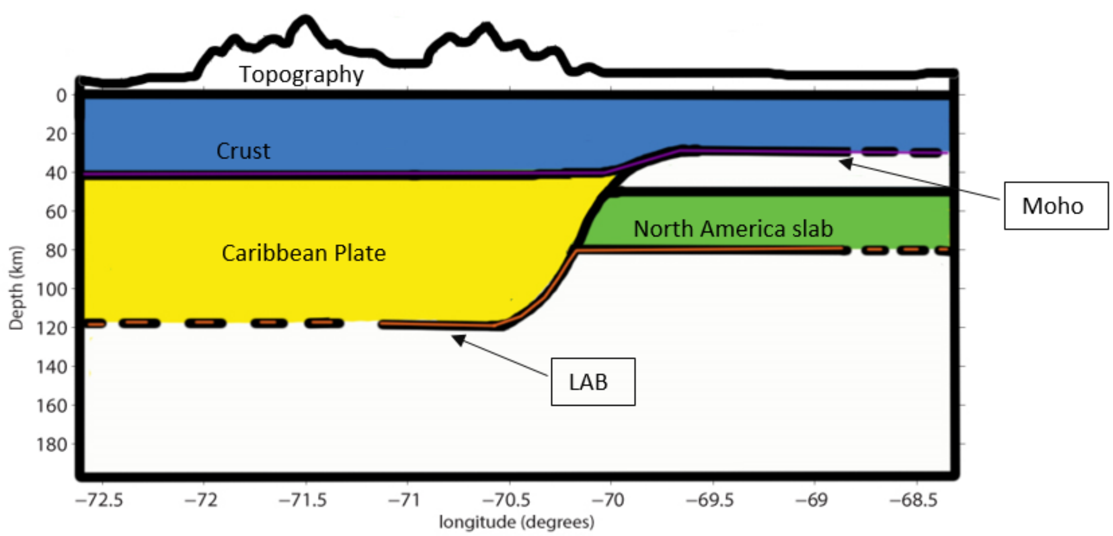

Figure 20. Cartoon illustration of the subsurface structures beneath Hispaniola based on our interpretation of migrated and stacked cross-sections. The subducting North American slab is pushing against the Caribbean plate lithosphere causing it to deform, which is evident on the surface topography as upthrusted mountains. The Moho boundary is traced in purple while the LAB is orange.

A laterally extensive LAB is notably absent in our P-wave receiver function image. The LAB is most commonly revealed in S-wave receiver functions. Unfortunately, we obtained poor results from SRF computations, which could have been due to a low data fold. (SRFs can only be computed for a narrow range of epicentral distances, due to interference by other phases, so SRF datasets are typically smaller than PRF datasets.) However, low quality SRFs in this region may also indicate that the seismically-determined "Lithosphere-Asthenosphere Boundary" (the primary target of SRF imaging) is poorly developed in this area. This is the most likely scenario in our study region, given its geologic history and ongoing tectonic activity. The Caribbean plate is composed of multiple geologic terranes, which accreted together during tectonic collisions of the plate with North and South America. Two major faults, the Septentrional to the north and the Enriquillo to the south divide present day Hispaniola into at least three geologically distinct zones. Figure 10 shows that the east-west cross-sections displayed in Figures 11-17 intersect the Septentrional at different longitudes. Therefore, the presence and location of the LAB is expected to change. Eastward of the island the lower contact of the NA slab acts as the LAB.

CHAPTER SIX

Conclusion

In this paper we used the P-wave receiver function technique to study the tectonic structure of the northeast Caribbean region. Using seismic data acquired in Hispaniola we were able to generate migrated and stacked images of the subsurface to a depth of 200 km. By interpreting the results based on the geological history of the region we found evidence for the slab push effect beneath eastern Hispaniola, which is associated with the North America (NA) slab's subduction beneath the northeast Caribbean. NA slab push against the Caribbean lithosphere may be a major driving force behind the ongoing deformation of Hispaniola, which is evident on the surface as a region of abrupt increase in elevation in central portion of the island. The earthquake hypocenters in the region could potentially serve as evidence for either Dolan et al.'s (1998) or Calais et al.'s (1992) hypothesis and a better understanding of the focal mechanisms of the earthquakes will help us resolve the issue. We failed to construct a reliable Sp RF image, which was as a result of poor S-wave receiver functions. We conclude that the poor SRFs could be either due to the restricted epicentral distance required for S receiver functions or because the LAB is not well-developed beneath Hispaniola, given that the region's active tectonics and multiple geological terranes. To resolve this, we would need to continue computing new SRFs as more data are recorded in the region. Additionally, seismic tomography using teleseismic and local arrivals would also allow us to gain insight into the volume and location of features. Features identified within the Ps receiver function image could be used to constrain the tomographic image; this should be the next major step in seismological studies of the Northeast Caribbean region.

REFERENCES

Agrawal, M., J. Pulliam, M. K. Sen, and H. Gurrola (2015), Lithospheric structure of the Texas-Gulf of Mexico passive margin from surface wavedispersion and migrated Ps receiver functions, Geochem. Geophys. Geosyst., 16, 2221–2239, doi:10.1002/2015GC005803.

Amukti, R., W. Suryanto, and Suharno., 2015. Subsurface Structure Model of Mount Merapi Using Receiver Function., Proceedings World Geothermal Congress

Bezada, M.J., A. Levander, and B. Schmandt, 2010. Subduction in the southern Caribbean; images from finite-frequency P wave tomography, J. Geophys. Res., 115(B12), doi: 10.1029/2010JB007682

Byrne, D. B., G. Suarez, and W. R. McCann., 1985, Muertos Trough subduction—Micro-plate tectonics in the northern Caribbean?, Nature, 317, 420–421. doi:10.1038/317420a0

Calais, E., Béthoux, N., and Mercier de Lépinay, B., 1992, From transcurrent faulting to frontal subduction: A seismotectonic study of the northern Caribbean plate boundary from Cuba to Puerto Rico: Tectonics, v. 11, p. 114-123

Coffin, M.F., Eldholm, O., 1994. Large igneous provinces crustal structures, dimensions and external consequences. Rev. Geophys. 32, 1e36. doi: 10.1029/93RG02508

Dewey, J. F., and J. L. Pindell (1986), Neogene block tectonics of eastern Turkey and northern South America; continental applications of the finite difference method; discussion and reply [modified]. Tectonics. 5(4). 703–705. doi:10.1029/TC005i004p00703

Dillon,W.P., J.A. Austin, K.M. Scanlon, N.T. Edgar, and L.M. Parson, 1992. Accretionary margin of north-western Hispaniola: morphology, structure, and development of the northern Caribbean plate boundary, Mar. Petrol. Geol., 9, 70–92.

Dolan, J. F., and D. J. Wald (1998), The 1943–1953 north-central Caribbean earthquakes: Active tectonic setting, seismic hazards, and implications for Caribbean-North American plate motions, in Active Strike-Slip and Collisional Tectonics of the Northern Caribbean Plate Boundary Zone, edited by J. F. Dolan and P. Mann, Geol. Soc. Am. Spec. Pap.,326, 143–169.

Dueker, K. G., and A. F. Sheehan, Mantle discontinuity structure beneath the Colorado Rocky Mountains and High Plains, J. Geophys. Res., 103, 7153 – 7169, 1998.

Gangopadhyay, A., J. Pulliam, and M. K. Sen (2007), Waveform modelling of teleseismic S, Sp, SsPmP, and shear-coupled PL waves for crust-and upper-mantle velocity structure beneath Africa, Geophys. J. Int., 170, 1210–1226.

Geman, S. & Geman, D., 1984. Stochastic relaxation, Gibbs distributions, and the Bayesian restoration of images, IEEE Trans. Patt. Anan. Mac. Int., 6, 721–741.

Giunta, G., M. Marroni, E. Padoa, and L. Pandolfi. 2003. Geological constraints for the geodynamic evolution of the southern margin of the Caribbean plate, in C. Bartolini, R. T. Buffler, and J. Blickwede, eds., The Circum-Gulf of Mexico and the Caribbean: Hydrocarbon habitats, basin formation, and plate tectonics: AAPG Memoir 79, p. 104– 125.

Govers, R., and R. Wortel, 2005. Lithosphere tearing at STEP faults: Response to edges of subduction zones, Earth Planet. Sci. Lett., 236, 505– 523, doi:10.1016/j.epsl.2005.03.022

Hansen, S., Dueker, K., 2009. P and S wave receiver function images of crustal imbrication beneath the Cheyenne belt in southeast Wyoming. Bull. Seismol. Soc. Am. 99, 1953–1961. doi:10.1785/0120080168

Kikuchi, M. and H. Kanamori (1982). Inversion of complex body waves, Bull. Seism. Soc. Am. 72, 491-506.

Kind, R., and L.P. Vinnik, The upper-mantle discontinuities underneath the GRF array from P-to-S converted phases, J. Geophys., 62, 138-147, 1988

Kirkpatrick, S., C.D, Gelatt., and M.P. Vecchi., 1983. Optimization by Simulated Annealing, Science, New Series, Vol. 220, No. 4598, 671-680

Kosarev, G., R. Kind, S. V. Sobolev, X. Yuan, W. Hanka, and S. Oreshin (1999), Seismic evidence for a detached Indian lithospheric mantle beneath Tibet, Science, 283, 1306 – 1309.

Langston, C. A. (1979). Structure under Mount Rainier, Washington, inferred from teleseismic body waves, J. Geophys. Res. 84, 4749-4762. doi:10.1029/JB084iB09p04749

Langston, C.A., 1977. Corvallis, Oregon, crustal and upper mantle structure from teleseismic P and S waves, Bull. seism. Soc. Am., 67, 713–724.

Li, X. Q., R. Kind, X. H. Yuan, I. Wolbern, and W. Hanka (2004), Rejuvenation of the lithosphere by the Hawaiian plume, Nature, 427(6977), 827–829, doi:10.1038/nature02349

Ligorria, J. P., and C. J. Ammon (1999), Iterative deconvolution and receiver-function estimation, Bull. Seismol. Soc. Am., 89, 1395–1400.

Mann, P., E. Calais, J. C. Ruegg, C. DeMets, P. E. Jansma, and G. S. Mattioli (2002), Oblique collision in the northeastern Caribbean from GPS measurements and geological observations, Tectonics, 21(6), 1057, doi:10.1029/2001TC001304.

Mann, P., Gahagen, L, and N. Grindlay, 2003. Early Miocene to Recent Plate Tectonic Animation of Highly Oblique Collision between the SE Bahama Carbonate Platform and the Puerto Rico-Virgin Islands-Hispaniola region, Seism. Res. Lett.. 74, 200, (plate animation)

Meighan, H. E., and J. Pulliam, 2013. Seismic anisotropy beneath the northeastern Caribbean; implications for the subducting North American lithosphere, Bulletin de la Societe Geologique de France, 184, Issue 1-2, pp. 67-76

Müller, R. D., Royer, J.-Y. & Lawver, L. A. 1993. Revised Plate Motions Relative to the hot spots from Combined Atlantic and Indian Ocean hot spot Tracks. Geology, 21, 275-278.

Niu, F., T. Bravo, G. Pavlis, F. Vernon, H. Rendon, M. Bezada, and A. Levander. 2007. “Receiver function study of the crustal structure of the southeastern Caribbean plate boundary and Venezuela.” Journal of Geophysical Research 112 (B11308). doi:10.1029/2006JB004802, 2007

Pindell, J. L. & Dewey, J. F. 1982, Permo-Triassic reconstruction of Western Pangea and the evolution of the Gulf of Mexico/Caribbean region, Tectonics, 1, 179-212. doi: 10.1029/TC001i002p00179

Rosencrantz, E., and P. Mann (1991), SeaMARC II mapping of transform faults in the Cayman trough, Geology, 19, 690–693. doi: 10.1130/0091-7613(1991)019<0690:SIMOTF>2.3.CO;2

Rosencrantz, E., M. I. Ross, and J. G. Sclater (1988). “Age and spreading history of the Cayman, Trough as determined from depth, heat flow, and magnetic anomalies.”J. Geophys. Res., 93(B3), 2141–2157. doi:10.1029/JB093iB03p02141

Sen, M. K., and P. L. Stoffa (1995), Global optimization methods in geophysical inversion, volume 4 of Advances in Exploration, Geophys., Elsevier, Amsterdam.

Sodoudi, F., R. Kind, D. Hatzfeld, K. Priestley, W. Hanka, K. Wylegalla, G. Stavrakakis, A. Vafidis, H.-P. Harjes, and M. Bohnhoff (2006), Lithospheric structure of the Aegean obtained from P and S receiver functions, J. Geophys. Res., 111, B12307, doi:10.1029/2005JB003932.

Szu, H. & Hartley, R., 1987. Fast simulated annealing, Phys. Lett., 122A, 157–162.

Vakil-Baghmisheh, M.-T., Peimani, M., Sadeghi, M. H., & Ettefagh, M. M. (2008). Crack detection in beam-like structures using genetic algorithms. Applied Soft Computing, Elsevier, Vol. 8, No. 2, pp. 1150-1160

van Benthem, S., R. Govers, and R. Wortel, 2014. What drives microplate motion and deformation in the northeastern Caribbean plate boundary region?, Tectonics, 10.1002/2013TC003402

van Benthem, S., R. Govers, W. Spakman, and R. Wortel, 2013. Tectonic evolution and mantle structure of the Caribbean, J. Geophys. Res. Solid Earth, 118, 3019–3036, doi:10.1002/jgrb.50235.

Vinnik, L.P., 1977. Detection of waves converted from P to SV in the mantle,Phys. Earth planet. Int., 15, 39–45.

Wilson, D. C., D. A. Angus, J. F. Ni, and S. P. Grand (2006). Constraints on the interpretation of S-to-P receiver functions, Geophys. J. Int. 165, 969–980, doi 10.1111/j.1365-246X.2006.02981.x

Yuan, X., R. Kind, X. Li, and R. Wang (2006). The S receiver functions: Synthetics and data example, Geophys. J. Int. 165, 555 – 564, doi 10.1111/j.1365-246X.2006.02885.x.

Yuan, X., S. V. Sobolev, R. Kind, O. Oncken, and Andes Seismology Group, New constraints on subduction and collision processes in the central Andes from comprehensive observations of P to S converted seismic phases, Nature, 408, 958 – 961, 2000

Zhu, L., Crustal structure across the San Andreas Fault, southern California from teleseismic converted waves, Earth Planet. Sci. Lett., 179, 183 – 190, 2000.